Composition-dependent structure evolution of FeVO₄ nano-oxide and its visible-light photocatalytic activity for degradation of methylene blue

Kgabo P. Thaba,[1,2] Mabel M. Mphahlele-Makgwane,[1,2] * Pannan I. Kyesmen,[3] Mmantsae Diale,[3] Priscilla G. Baker, [5] Peter R. Makgwane [4,5] *

[1] *Department of Water and Sanitation, Private Bag X1106, University of Limpopo, Sovenga, 0728, South Africa.*

[2] *Department of Chemistry, Private Bag X1106, University of Limpopo, Sovenga, 0728, South Africa.*

[3] *Department of Physics, University of Pretoria, Private Bag X20, Hatfield 0028, South Africa*

[4] *Centre for Nanostructures and Advanced Materials (CeNAM), Council for Scientific and Industrial Research (CSIR), Pretoria, 0001, South Africa.*
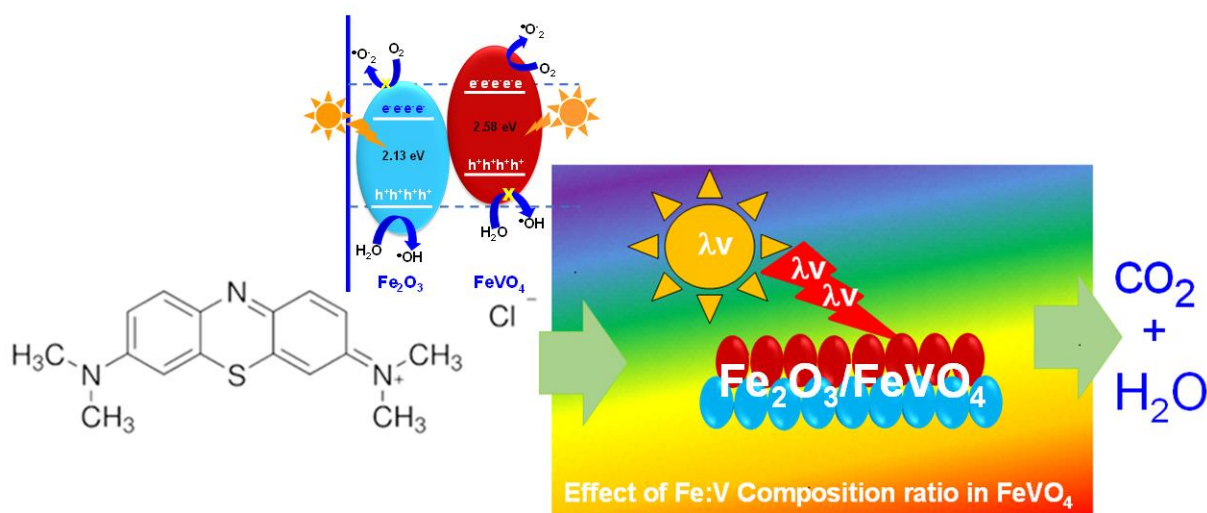
[5] *Department of Chemistry, University of the Western Cape, Bag X17, Robert Sobukwe Drive, Bellville, 7535, South Africa.*

*Correspondence authors:

Email: mabel.mphahlele-makgwane@ul.ac.za; makgwane.peter@gmail.com

Tel: +27152033498; Fax: +27152035979

Graphical Abstract

Abstract

This work report on the synthesis of the iron orthovanadate oxide ($FeVO_4$) catalysts with various vanadium (V) loading amounts of 10% (FeV-1); 20 wt% (FeV-2); 30 wt% (FeV-3) and 40 wt% (FeV-4). The structure evolution of $FeVO_4$ was studied by using XRD, UV-vis, PL, FTIR, XPS, SEM, EDX, TEM, EIS, Raman and BET surface area techniques. XRD analysis showed that crystal structure and phase formation of $FeVO_4$ to depend on V-metal loadings, and that the various Fe:V ratio showed peaks shifting, which were related to the transformation of Fe_2O_3 and V_2O_5 interface into $FeVO_4$ phase with respect to increasing V-metal loadings. The XPS results showed the significant influence of the V-metal loadings on inducing various electronic, redox oxidation states of $V^{3+}/V^{4+}/V^{5+}$ and Fe^{2+}/Fe^{3+} and oxygen vacancy defects structure properties of $FeVO_4$ catalysts. The physical structure changes confirmed by XRD, XPS and FTIR manifested the tailoring of the optical properties as evidenced by PL and UV-vis with FeV-3 catalyst showing the desirable optics properties. This were determined to give the properties for the efficient photodegradation activity of methylene blue model organic dye of wastewater with its near complete removal with 30 min reaction time. The enhanced productivity photodegradation performance of the hetero-mixed $FeVO_4$ catalysts is ascribed to their enriched visible-light harvesting range and efficient suppression of electrons/holes (e^-/h^+) recombination manifested by the effect of Fe:V composition ratio. Moreover, the presence of small quantity of Fe_2O_3 in predominant $FeVO_4$ could allow efficient e^-/h^+ separation and transfer by creation of $Fe_2O_3/FeVO_4$ heterojunction interface. The $FeVO_4$ catalyst showed excellent recyclability and its stable photoactivity under aqueous degradation conditions.

Keywords: *Photocatalyst; iron-orthovanadate ($FeVO_4$); photodegradation; methylene blue.*

1. Introduction

The application of organic dyes in the textile industry for coloring fabrics dates to the Neolithic period and it constitutes the core of the modern textile manufacturing industries. Unlike in the old days with the use of plant extracted dyes, nowadays the textile industry relies extensively on synthetic of organic dyes [1]. The main problems associated with the use of these synthetic dyes is their release into the water ecosystem, thus presenting a detrimental impact of accessing clean water. As a result, the prominent solution is to remove the dyes in the effluents wastewater streams at the generation source before being released into the ecosystem to be exposed to clean water [2]. Several methods have been reported as means for treatment removal of organic dyes in textile contaminated wastewater streams including adsorption [3], electrocoagulation [4], biodegradation [7] and advanced oxidation processes (AOPs) using Fenton and photodegradation [8,9] techniques. Photocatalysis offers effective methods for the

complete degradation of organic dyes to carbon dioxide (CO_2) and H_2O as compared to other methods that usually creates accumulation of secondary pollutants. The use of photocatalysis in the degradation removal of organic dyes has been the most extensively studied. Enormous research is directed towards further development with respect to the design of new material photocatalysts to achieve efficient photodegradation processes [10]. On the other hand, the success application of photocatalysis depends on the design of materials that can fulfill the desired properties including extended visible light absorption, effective photo-generation of charge carriers, separation, and transfer for their utilization on redox photodegradation of organic dye molecules [11]. The common traditional metal oxides such as TiO_2, ZnO, SnO_2, CeO_2 and ZrO_2 are only active in the ultraviolet (UV) light, which constitute only 4%, hence this hampers their use in the simulated or direct solar sunlight degradation of dyes over an extended visible spectrum region [10-17]. Both vanadium and iron oxide respectively and combined are capable of visible light absorption which is 39% or above of the solar sunlight composition, thus they could present effective degradation efficiencies as heterostructured designed photocatalyst [18,19].

Hetero-mixed interfaces of more than two metal oxides have been the most effective strategies in designing visible-light photoactive materials [20,21]. At the interface junctions of mixed metal oxides, there are several intrinsic structural properties improvement with respect to extended solar light absorption range to visible with enhanced efficiency to generate, separate and transport charge carriers for effective redox utilization in photocatalytic reactions [22-28]. These photocatalytic mechanisms can be significantly improved at composite oxides interfaces by creating oxygen vacancies defects, which can act as electrons sites trapping while improving redox activity adsorption/desorption of the reacting substrates [29-30]. To demonstrate the significant photocatalytic enhancement in hetero-mixed metal oxides, several metal orthovanadates (AVO_4) (A = metal oxide) based on $BiVO_4$ [31], $CeVO_4$ [32], $LaVO_4$ [33], $InVO_4$ [34], $GdVO_4$ [35], and $PrVO_4$ [36] semiconductors have been successfully synthesized, characterized, and evaluated for their photocatalytic structure properties. Amongst these orthovanadates, iron orthovanadates ($FeVO_4$) constituting the heterostructure composite of iron and vanadium is photoactive under both UV and vis light due to its narrow band gap energy of 2.02–2.7 eV [37]. Because of its visible-light photoactivity, $FeVO_4$ has demonstrated relatively effective degradation activity in removal of organic wastewater contaminants compared to Fe_2O_3 which requires the addition of H_2O_2 to be active under UV and vis light [38,39]. Moreover, several strategies have been reported for the synthesis of $FeVO_4$ based catalysts and evaluation of their photocatalytic activity in the degradation of various organic dyes [40-42]. The photocatalytic activity of $FeVO_4$ is limited by its low adsorption capability range (approximately 500 nm wavelength) and high recombination rates of electrons (e^-) and holes (h^+) pair [43]. The influence of $FeVO_4$ catalysts structural aspects such as morphology, shape,

size, dopants and heterojunctions interfaces on the charge carrier's separation and transport efficiencies with the view to optimize the structure-activity photocatalytic performance have been investigated [44-47]. One aspect that has not been explored in the literature is the influence of Fe and V compositions ratios on both structure-activity performance relationships of $FeVO_4$ photocatalysts with respect to the optical absorbance properties under visible light region and its photodegradation activity. As a result, herein, we investigated the effect of various Fe and V compositions ratio with increasing loading amounts of V-metal from low to high loadings with respect to their photodegradation activity in the removal of methylene blue. The understanding of the effect of various V-metal loadings could be beneficial in understanding the basis photocatalytic properties of optimized binary $FeVO_4$ catalysts for further developments in heterostructured photocatalysts.

2. Experimental Methods

2.1 Catalysts synthesis

For synthesis of $FeVO_4$ catalysts with different V-metal loadings, the required amounts of vanadium pentoxide (V_2O_5) and of iron nitrate nonahydrate ($Fe(III)(NO_3)_2 \cdot 9H_2O$) were added into 250 ml flask containing 100 ml mixture of ethylene glycol (EG) and deionized water (H_2O) solvent with ratio of 3:1. The amounts of vanadium were varied relatively to be 10 wt%, 20 wt%, 30 wt% and 40 wt% with respect to 25 mmol of $Fe(III)(NO_3)_2 \cdot 9H_2O$. This solution mixture was stirred at 100 °C for 1 h under reflux and followed by the dropwise addition of HNO_3 until the pH was 2-3 with the continuous stirring of the reaction mixture for another 1h. Thereafter, a 0.5 g of PVP surfactant, which was initially dissolved completely in 20 mL of H_2O, was added dropwise. After allowing the reaction solution mixture to homogenize under 100 °C for 30 min under reflux, the pH was adjusted to 9 using aqueous NH_4OH. The reaction solution mixture was stirred continuously at 100 °C under reflux for 24 h. After 24 h, the reaction solution was allowed to cool, and the resulting slurries of the catalysts were collected by centrifugation and then washed with the mixture of ethanol/water (1:1) for several times. The obtained solid catalysts were then dried at 110 °C for overnight in an oven. The obtained $FeVO_4$ catalysts depending on nominal V loadings were denoted as FeV-1 (10 wt% V); FeV-2 (20 wt% V); FeV-3 (30 wt% V); and FeV-4 (40 wt% V), respectively. Similarly, Fe_2O_3 was synthesized following the same procedure without vanadium while commercial V_2O_5 was used.

2.2 Catalysts characterisation

The crystalline structures and phases of the synthesized catalysts powders were recorded using the powder X-ray diffraction (XRD) (PANalytical X'PERT-PRO diffractometer, Netherlands) operated at

tube voltage and current of 45 kV and 40 mA, respectively. The primary X-rays from Ni filtered CuKα radiation was set at 0.154 nm with the scan range of 2θ = 20–90 ° using continuous scanning at a rate of 0.02 °/s. The surface areas and pore distributions of the samples were analyzed on a Micromeritics BET surface area and porosity analyzer (Tri-Star II 3020, USA) by using nitrogen (N_2) physisorption at -196 ºC and calculated by the Bruner-Emmer-Teller (BET) and Barret-Joyner-Halenda (BJH). The morphologies, dimension and elemental compositions of the prepared catalysts samples were characterized by Scanning electron microscopy (SEM) with the images recorded on a Zeiss-Auriga focused-ion-beam (FIB) operated at accelerating voltage of 3 keV coupled to energy dispersive X-ray (EDX). The ultraviolet-visible (UV/Vis) spectroscopy technique was used to investigate the light absorption edges of the catalysts to gain insight into the visible-light response recorded using the Perkin Elmer Lambda 750 UV/Vis spectroscope at wavelength from 200 to 1200 nm. The raw data were resolved using the Perkin Elmer UV WinLab™ software. The photoluminescence (PL) technique was used to determine the charge recombination of the catalysts by measuring them on HORIBA Jobin Yvon Nanolog® spectrofluorometer at excitation wavelength of 325 nm. The emission peaks were recorded at wavelength ranging from 350–700 nm. The oxidation states and binding energy of the photocatalysts were collected by X-ray photoelectron spectroscopy (XPS) using Kratos Axis Ultra device (Kratos, United Kingdom), which used monochromatic (Al Kα) as the excitation source. Electrochemical measurements were done using a VersaSTAT 3F potentiostat from Princeton Applied Research, in a three-electrode setup. 10 mg of each of the prepared nanoparticles were dissolved in 10 ml of deionized water and sonicated for 30 min to form a homogeneous solution. 10 µL of the solution was dropped on glassy carbon (GC) electrode and dried in an oven at 80°C for 10 mins. About 3 µL of 5% Nafion, which served as a binder was then dropped on the GC electrode and dried for 5 min. Electrochemical impedance spectroscopy (EIS) was performed on the samples where the modified GC electrode, 2×2 cm platinum mesh, and Ag/AgCl in 3M KCl served as working, counter, and reference electrodes respectively. 0.1M of N_2-bubbled Na_2SO_4 was used as the electrolyte. The EIS studies were done at a frequency range of 0.1 to 10 000 Hz, an amplitude of 10 mV, and a potential of 0.4 V vs. Ag/AgCl. Raman spectroscopy study of the films were performed using a WiTec alpha 300 RAS+ Confocal Raman Microscope with excitation laser of 532 nm at 5 mW.

2.3 Photocatalytic degradation activtiy studies

Catalytic activity testing of the materials for the photodegradation of the methylene blue (MB) was performed at near room temperature (26 ºC) using a sealed stirred batch glass photo-reactor with the capacity volume of 1 L. The typical test solutions consisted of 500 mL of aqueous MB dye solution with 10 ppm or 10 mg/L concentration, and 100 mg of catalyst. Before illumination of the reactor, the MB

dye test solution was placed in dark for 30 min under continuous stirring to allow for adsorption-desorption equilibrium. A visible light 350 W Xenon lamp using a desired wavelength (nm) with the cut-off filter ($\lambda > 420$) to remove UV radiation under stirring irradiated the dye solution mixture. Liquid samples of the reaction mixture were withdrawn periodically and filtered solid catalyst before analysis of on UV-vis absorption spectrophotometer to monitor the progression of the degraded amount of MB dye.

3. Results and discussion

3.1. Catalysts characterisation

Fig. 1(a) and Fig. 1(b) shows the XRD structure patterns of the $FeVO_4$ based catalysts. The iron oxide shows the formation of strong diffraction peaks at $2\theta = 24.1°(012)$; $33.2°(104)$; $35.7°(110)$; $40.9°(113)$; $49.5°(024)$; $54.1°(116)$; $57.5°(018)$; $62.4°(214)$; and $64.1°(300)$ with respective planes belonging to the hematite Fe_2O_3 phase (JCPDS No. 89-0599) [19]. The XRD patterns confirming V_2O_5 is shown in Fig. S1 (supporting information). For $FeVO_4$ catalysts, the intensities of their XRD peaks varied relatively with the increasing amounts of V-metal loadings from FeV-1 to FeV-4 (Fig. 1b). The decrease of Fe_2O_3 peak intensity at 2θ of $24.1°$ (012) disappeared at higher V-metal loadings for FeV-3 and FeV-4 (Fig. 1b). The FeV-2, FeV-3 and FeV-4 catalysts shows the appearance of new XRD peaks at 2θ of 24 - 28° (Fig. 1b). These peaks correspond to (012), (112), and (221) planes due to $FeVO_4$ phase (JCPDS No. 71-1592) [37,40,41]. At low V-metal loadings (FeV-1 with 10 wt%) the XRD peaks due to $FeVO_4$ phase are not well defined, hence Fe_2O_3 peaks are dominant. Moreover, the Fe_2O_3 XRD peaks at 33.16° and 35.65° shows shifting to high 2θ due to the introduction of the vanadium into its structures, thus indicating strong interactions of the two metals. The peaks shifts can be correlated to the particles size of vanadium, where its introduction of nanosized particles comparable to that of Fe_2O_3 will occupy the interstitial position, which can lead to changes in the lattice structure and the *d*-spacing between the atoms to become less, hence the increase in the XRD peaks shifting to higher angles [41].
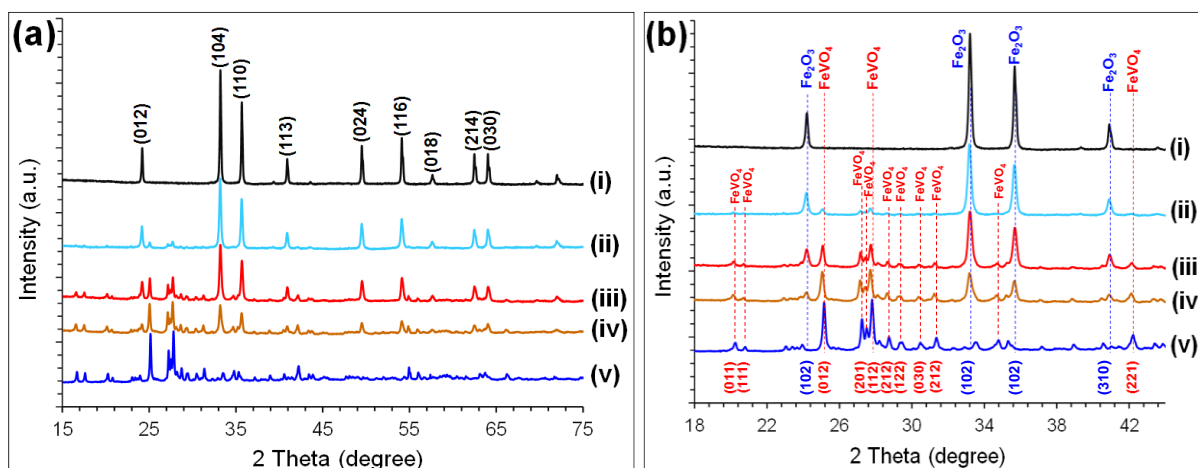
Fig. 1. XRD of the FeVO$_4$ catalysts (a) full 2θ scale (b) magnified 2θ = 22–44° range. (i) Fe$_2$O$_3$; (ii) FeV-1; (iii) FeV-2; (iv) FeV-3; and (v) FeV-4.

Fig. 2 shows the sorption isotherms of FeVO$_4$ catalysts. The FeVO$_4$ catalysts shows type IV isotherm curve shape that are mesoporous with hysteresis loop of H1-type based on the IUPAC classification [48]. The BET surface areas (SA_{BET}) of FeVO$_4$ catalysts are low compared to 72.0 m^2/g of Fe$_2$O$_3$. Further, V$_2$O$_5$ shows relatively low surface area of 8.6 m^2/g. The SA_{BET} of the catalysts shows to decrease from 57.0 m^2/g (FeV-1) to 21.7 m^2/g (FeV-4) for FeVO$_4$ catalysts with respect to increase of V$_2$O$_5$ loading from 10 to 40 wt% (Table 1). The average pore size diameters (D_{pore}) of FeVO$_4$ catalysts are in the range of 19–42 nm (Table 1) while their distribution range over the diameter size of 5–100 nm (Fig. 2). Similarly, the pore volume (V_{pore}) capacity of the catalysts varies in the range of 0.07–0.40 cm^3/g (Table 1). The results show that the mesoporous structure of FeVO$_4$ is re-constructed by the dispersion of various V$_2$O$_5$ loadings onto Fe$_2$O$_3$, especially for the high V-metal loading amounts.
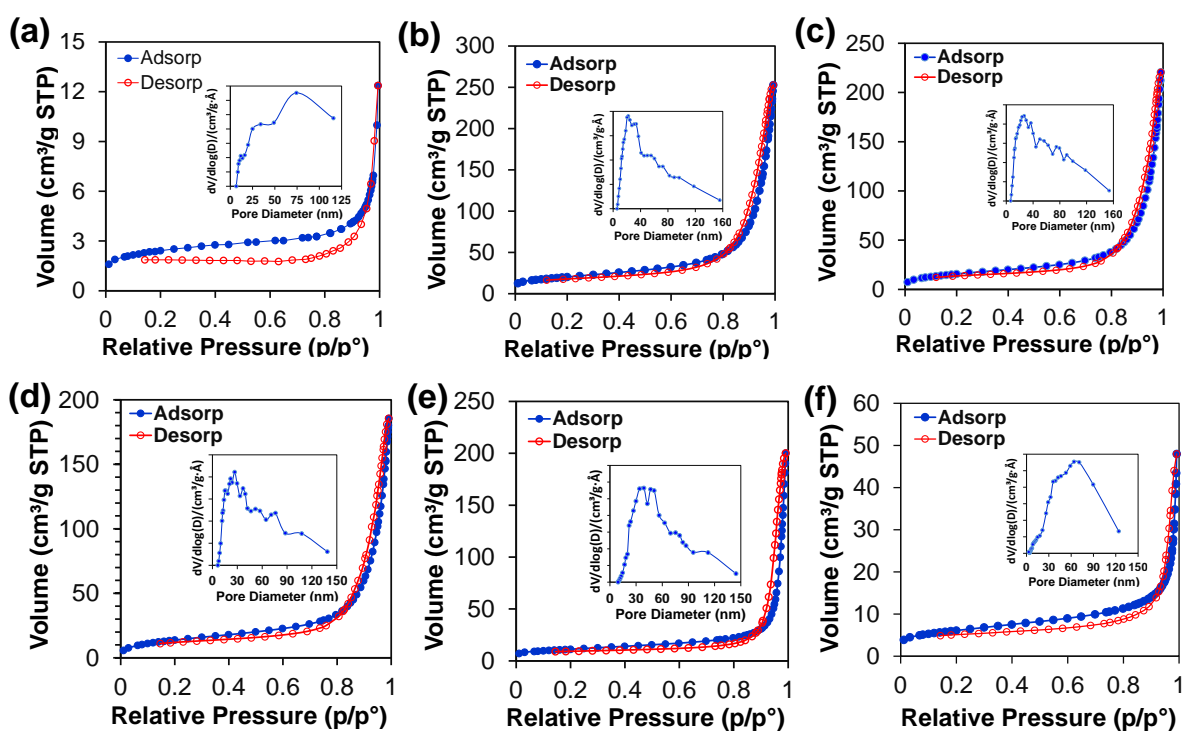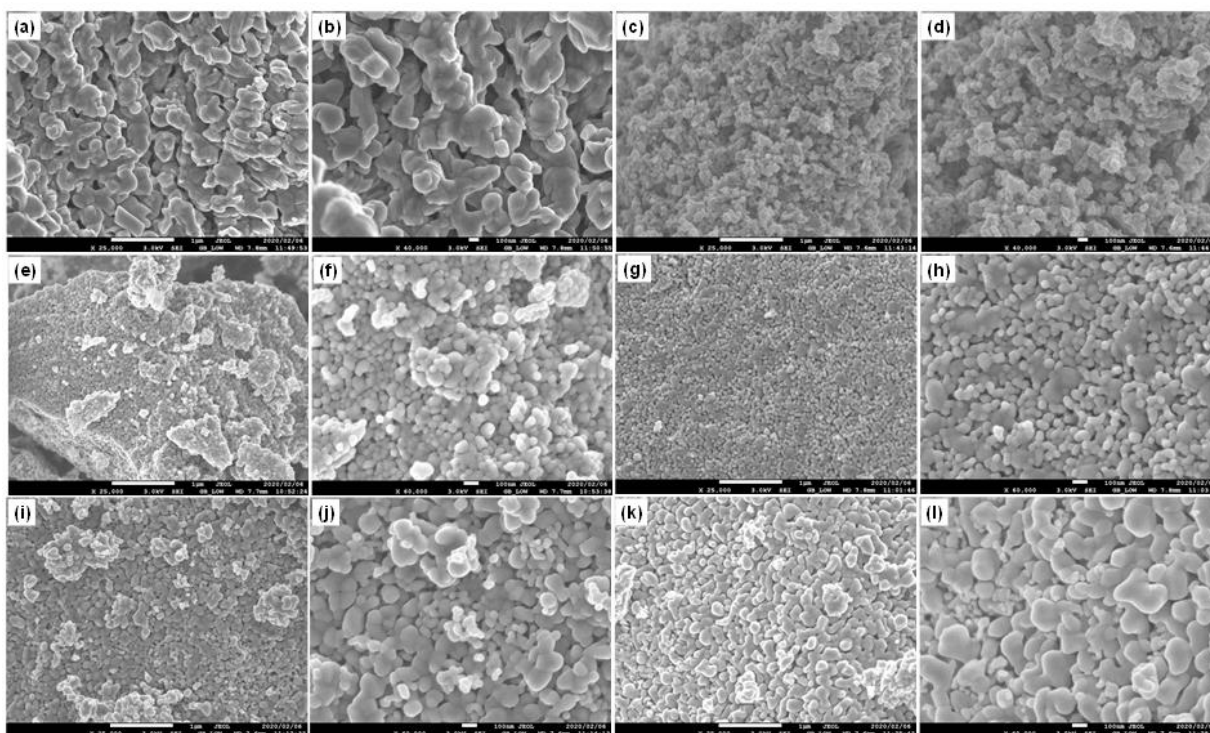
Fig. 2. N_2 physisorption and pore size curves of $FeVO_4$ catalysts. (a) V_2O_5; (b) Fe_2O_3; (c) FeV-1; (d) FeV-2; (e) FeV-3 and (f) FeV-4.

Table 1. BET surface area, pore size dimeter and volume of the $FeVO_4$ catalysts.

Entry	Catalyst	SA_{BET} (m²/g)	D_{pore} (nm)	V_{pore} (cm³/g)
1	Fe_2O_3	72.0	24.12	0.313
2	V_2O_5	8.6	19.20	0.018
3	FeV-1	57.0	26.60	0.345
4	FeV-2	50.7	25.59	0.324
5	FeV-3	46.8	41.64	0.394
6	FeV-4	21.7	19.28	0.073

Fig. 3. SEM of FeVO$_4$ catalysts. (a)-(b) V$_2$O$_5$; (c)-(d) Fe$_2$O$_3$; (e)-(f) FeV-1; (g)-(h) FeV-2; (i)-(j) FeV-3; (k)-(l) FeV-4.

Fig. 3 illustrates the SEM microstructure images of the binary FeVO$_4$ based catalysts including Fe$_2$O$_3$ and V$_2$O$_5$. V$_2$O$_5$ shows its morphology to compose of agglomerated large irregular sharped particles with approximate diameter size of larger than 100 nm with poorly defined pores shapes (Fig. 3a-3b). On the other hand, the morphology of Fe$_2$O$_3$ shows uniform porous small nanoparticles (NPs) with diameter size of less than 20 nm (Fig. 3c-3d). The FeV-1 catalyst consist of spherical-shaped NPs morphology with the diameter size of 20–30 nm. The spherical NPs morphology of FeV-1 shows agglomerations and an increase in size for FeV-2 and FeV-3 (Fig. 3). In the FeV-4 sample, the spherical NPs morphology observed in for FeV-1 to FeV-3 shows to transform completely into uniform loosely bound large NPs of greater than 100 nm in diameter size. The elemental mapping of the FeVO$_4$ catalysts is summarized in Fig.'s S2–S7 (Supporting Information) with the corresponding Fe and V elemental amounts in Tables S1–S6 (Supporting Information). The FeVO$_4$ catalysts shows well distribution of the Fe and V elements. The tentative amounts of V-metal in the FeVO$_4$ catalysts were as follows: FeV-1 (V= 7.02 wt%); FeV-2 (V= 14.70 wt%); FeV-3 (V= 27.07 wt%); and FeV-4 (V= 34.72 wt%). The TEM was employed to investigate the nanostructure morphology and particles size of the FeVO$_4$ based catalysts. The TEM images and associated single angle electron diffraction (SAED) rings of the respective catalysts, Fe$_2$O$_3$ and FeVO$_4$ based are illustrated in Fig. 4. The Fe$_2$O$_3$ shows the formation of agglomerated nanosized

9

particles with tentative diameter size of 10–15 nm (Fig. 1a). Further, the SAED of Fe_2O_3 confirms the polycrystalline rings which correlates well with the XRD resolved crystalline peaks (Fig 1a). For V-metal loaded $FeVO_4$ catalysts (FeV-1 and FeV-3), the < 15 nm nanoparticles size obtained for the pure Fe_2O_3 had increased to a range diameter size of 20-50 nm. This increase of large particles size in $FeVO_4$ based catalysts is because of vanadium as reported previously for vanadium supported or heterostructure catalysts materials [49-52]. Furthermore, the same trend observed in the TEM increase in particle size of $FeVO_4$ catalysts with V-metal loadings when compared to Fe_2O_3 is correlated with respective changes in SEM particles morphology results (Fig. 3c-3l). The resolved SAED ring patterns for Fe_2O_3 is only observed in low concentration loaded $FeVO_4$ catalyst (FeV-1) compared to scattered in FeV-3 due to high vanadium loading and transformation into new phase of $Fe_2O_3/FeVO_4$.
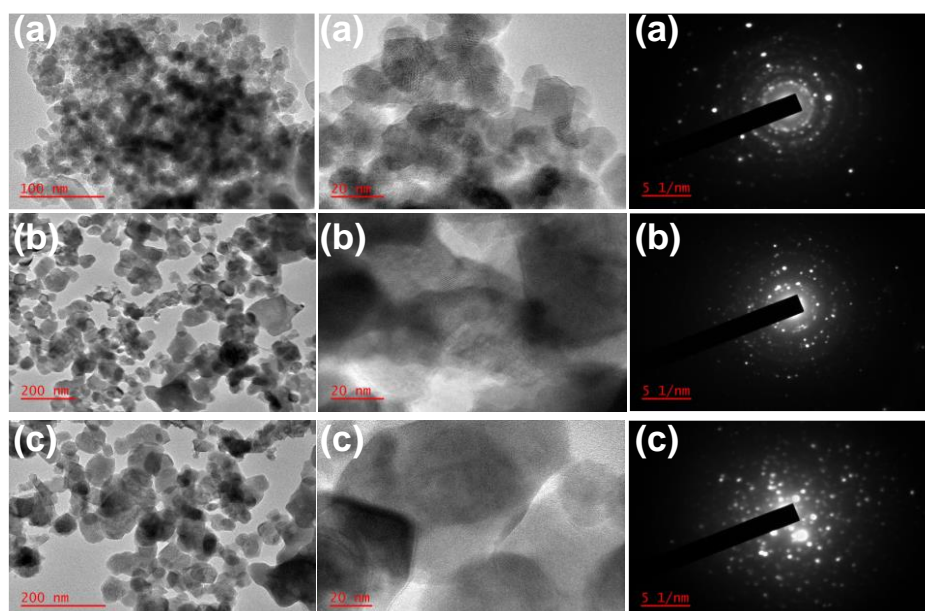
Fig. 4. TEM images and SAED of (a) Fe_2O_3; (b) FeV-1 and (c) FeV-3 catalysts

Fig. 5a presents the UV-vis optical structure properties of the pristine Fe_2O_3 and $FeVO_4$ based catalysts. All the $FeVO_4$ catalysts showed the increase in visible-light absorption range due to the strong red shift in comparison to Fe_2O_3, which indicates the prominent efficiency in photoinduced generation of more e^-/h^+. The respective optical band gap (E_g) of Fe_2O_3 and $FeVO_4$ based catalysts are illustrated in Fig. 5b. The E_g optical values estimated according to absorption spectrum of respective $FeVO_4$ and Fe_2O_3 catalysts calculated by equation $E_g = 1240/\lambda_{Abs.Edge}$ and resolved using the Kulbelka-Munk function $[F(R)h\nu]_{1/2}$ are shown in Fig. 5b. The different band gap values are as follows: Fe_2O_3 (2.13 eV); FeV-1

(2.47 eV); FeV-2 (2.51 eV); FeV-3 (2.58 eV), and FeV-4 (2.69 eV). The obtained band gap values for Fe_2O_3 catalysts are correlated to previously reported [53-55].
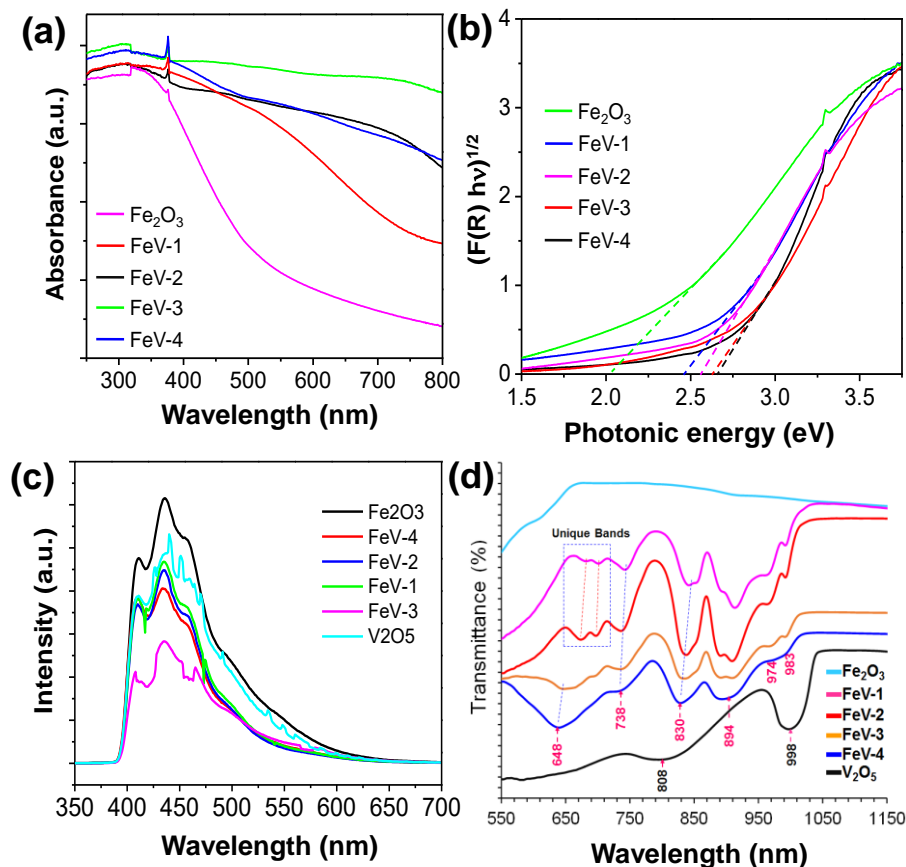

Fig. 5. (a) UV-vis curves; (b) Tauch band gap energies; (c) PL curves; and (d) FTIR of the FeVO$_4$ catalysts.

Fig. 5c shows the PL curves of V_2O_5, Fe_2O_3 and FeVO$_4$ catalysts. When a semiconductor photocatalyst is illuminated by light it generates e^-/h^+ charge photocarriers that recombine, and some of e^-/h^+ photocarriers release energy in the form of fluorescence emission. Hence, the lowest fluorescence emission intensity indicates low or highly suppressed e^-/h^+ recombination rate, thus efficient e^-/h^+ separation [56]. All the FeVO$_4$ catalysts including their respective single Fe_2O_3 and V_2O_5 shows light absorbance capacity within the 400–600 nm wavelength range. Further, all the catalysts show the most intense high PL emission peak at approximately 450 nm wavelength. The PL intensity of FeV-3 catalyst at 450 nm was the lowest, which implies its best separation and suppression recombination efficiency of the charge carriers [31]. It is also observed that the PL intensity of FeVO$_4$ catalysts decreased with the increase in vanadium content from FeV-1 to FeV-3, which indicated their reduced probability of e^-

/h$^+$ recombination in the valence band (Fig. 5c). However, the higher PL peak intensity is observed for FeV-4 catalyst, which could be due to the high V$_2$O$_5$ loading amount since pure V$_2$O$_5$ had the higher peak intensity than FeV-4 (Fig. 5c). This shows that there is the optimum loading amount effect of V-metal in the binary FeVO$_4$ catalysts to achieve the best photo-generation of e$^-$/h$^+$ and their transfer with the high separation efficiency for the enhanced photocatalytic activity rates.

Fig. 5d shows the FTIR spectrum of the FeVO$_4$ catalysts measured in a range of 550–1150 cm^{-1}. For V$_2$O$_5$, the resolved IR band at 998 cm^{-1} is ascribed to the vibration mode of the V=O bond and the absorption peaks between 750–850 cm^{-1} are attributed to the bridging oxygen atoms of the V-O-V bond [56]. Fe$_2$O$_3$ shows not well-resolved IR bands appearing at 600–700 cm^{-1}. For FeVO$_4$ catalysts, the different IR bands are observed with respect to the changes in the molar ratio compositions of V and Fe metals content. The IR bands with the broad peaks at 550–700 cm^{-1} are due to the vibration modes of V-O-Fe and V-O-Fe mixed bridging stretching [56]. Further, the IR bands at 850–1050 cm^{-1} are ascribed to the vibration mode stretching of the short vanadyl (V-O) bonds. The IR band at 894 cm^{-1} is due to the V-O and V-O-V coupled vibration modes while at 830 cm^{-1} is due to the bridging V-O$^{..}$Fe stretching [57,58]. The IR bands at 974–983 cm^{-1} depicts number of vibration modes peaks, which shows to decrease relatively with the increase in V$_2$O$_5$ loadings while leading to the formation of new broader bands that are due to the Fe-O and Fe-O-Fe. The shift of the band at 830 cm^{-1} to lower wavenumber originates from the relative increase in V$_2$O$_5$ loading from FeV-1 to FeV-4.
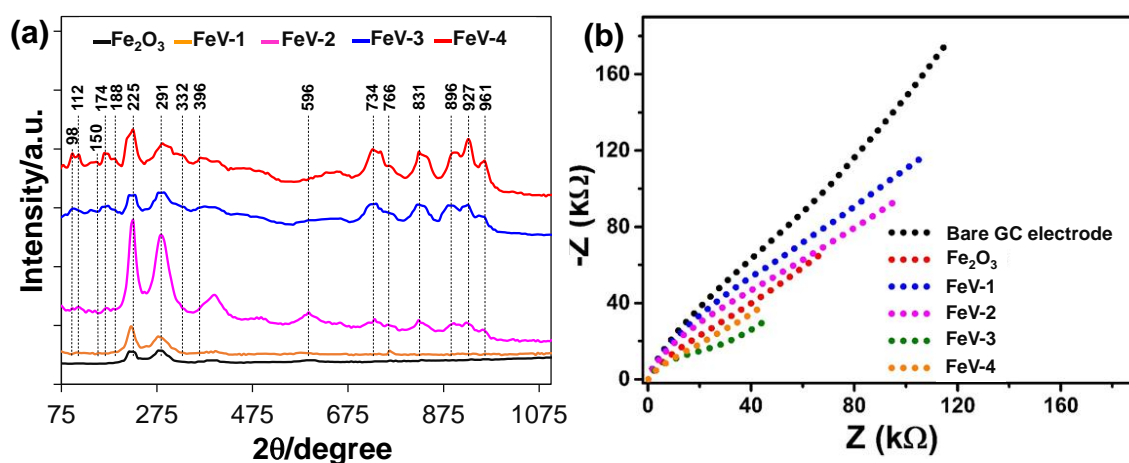

Fig. 6. (a) Raman spectra and (b) Electrochemical impendence spectroscopy curves.

Fig. 6a shows the Raman spectra bands patterns of Fe$_2$O$_3$ and FeVO$_4$ based catalysts. The peaks at 225 and 291 cm^{-1} confirms the Fe$_2$O$_3$, which corresponds to E$_{1g}$ and $_{A1g}$ bands, respectively. These peaks,

especially at 225 and 291 cm^{-1} are observed in the FeVO$_4$, thus indicating the formation of heterostructure Fe$_2$O$_3$/FeVO$_4$. The Raman bands of FeVO$_4$ are clearly resolved for FeV-2, FeV-3 and FeV-4 catalysts while FeV-1 showed mainly strong peaks due to Fe$_2$O$_3$ except one band at 761 cm^{-1}. The low detection of peaks due to FeVO$_4$ in FeV-1 indicate the high dispersion of vanadium metal for low loadings [49]. The bands at 332 and 362 cm^{-1} are due to the VO$_4$ symmetric and asymmetric bending.

The electrochemical impedance spectroscopy (EIS) analysis was performed to study the resistivity and the charge transfer kinetics at the surface of the FeVO$_4$ based catalysts. Fig. 6b illustrates the obtained Nyquist plots of the measurements conducted on the modified and bare GC electrodes. The plots revealed partial semicircles at higher frequencies followed by a line at lower modulations which often represent a much larger circle. Smaller semicircles depict a decrease in charge transfer resistance at the surface of the semiconductor material [59]. All the modified GC electrodes with Fe$_2$O$_3$ and FeVO$_4$ catalysts yielded smaller semi-circles compared to the bare one as expected because of the higher electron transfer at their surfaces due to the modification with photocatalysts nanoparticles. The FV-3 photocatalyst showed the least resistance to electron transfer at its surface followed by FeV-4 sample. The improved conductivity observed for FeV-3 correlated well with the PL results, which showed FeV-3 with less charge recombination rates, thus efficient separation and transfer of photocarriers for their effective redox utilization in the degradation reaction. Similarly, FeV-1 showed the highest surface resistance to charge transfer because of its high charge recombination rates as shown by the PL (Fig.5c). The FeVO$_4$ nano-oxide catalyst with the least charge transfer resistance will usually result in better electrochemical charge mobility performance in the photo-degradation of organic dye molecules.
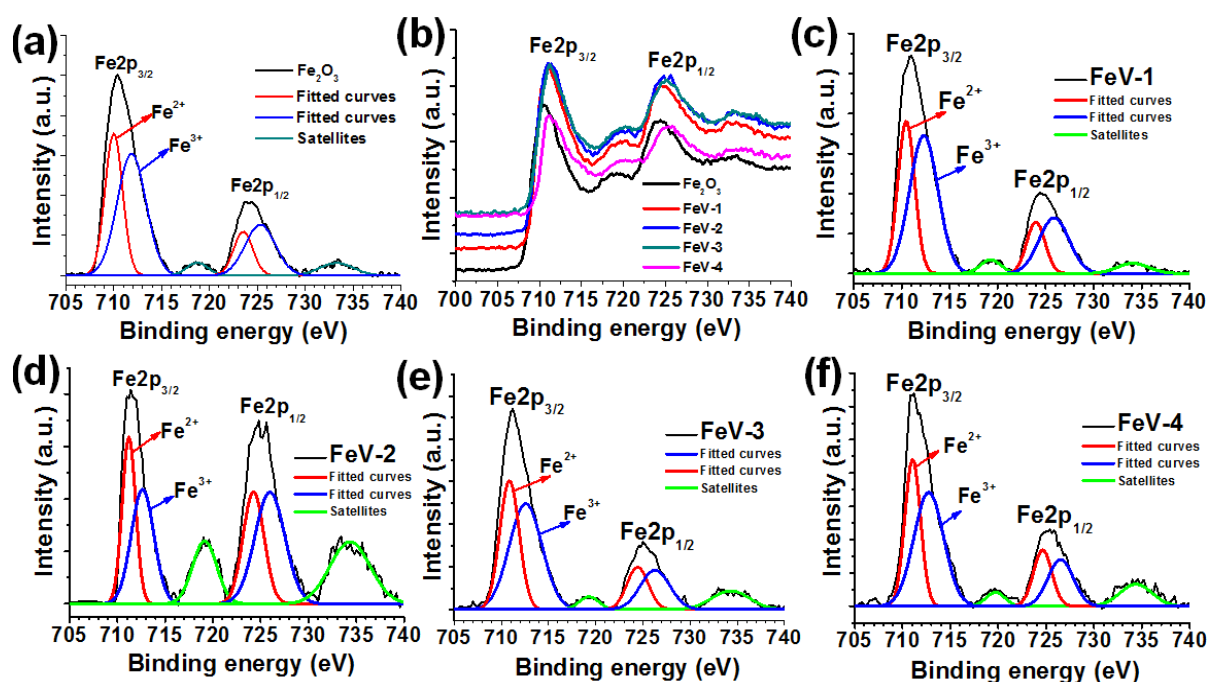
Fig. 7. Fe 2p XPS of (a) Fe_2O_3; (b) Overlaid comparison of all $FeVO_4$ catalysts; (c) FeV-1; (d) FeV-2; (e) FeV-3; and (f) FeV-4 catalysts.

The XPS survey scan of the $FeVO_4$ catalysts are illustrated in Fig. S8. The survey spectra confirm the presence of the Fe, V and O elements in the binary $FeVO_4$ catalysts. The XPS Fe 2p spectra of Fe_2O_3 shown in Fig. 7a shows the two peaks with the binding energies (BE) at 710.0 eV and 724.5 eV. These peaks are due to the spin-orbit coupling of Fe $2p_{3/2}$ and Fe $2p_{1/2}$, respectively (Fig. 7a) [37-39,60,61]. Further, the XPS spectra of Fe_2O_3 confirms the Fe^{2+}/Fe^{3+} redox pair to be slightly more in the low oxidation state of Fe^{2+}. The other small peaks at BE of 720 eV and 735 eV are satellite peaks of the Fe_2O_3 [61]. For $FeVO_4$ catalysts, their overlaid Fe 2p in Fig. 5b shows the peaks shifting with respect to pure Fe_2O_3 to higher BE region for both Fe $2p_{3/2}$ and Fe $2p_{1/2}$, respectively. The Fe 2p peaks shifting in the $FeVO_4$ catalysts did not show to follow any significant trend due to the different vanadium loadings. These peaks shifting corroborate the results obtained in the XRD and FTIR where the different phases compositions and vibration modes of interactions were observed relative to the various amounts of V-metal loadings in the $FeVO_4$ catalysts. The non-existence of the well-defined trend is ascribed due to the possible formation of the difference phases of vanadium species manifested by the V-metal loadings. The fitted Fe 2p peaks of the $FeVO_4$ catalysts shows similar trend of the composition ratio of Fe^{2+} and Fe^{3+}, where Fe^{2+} was the dominant oxidation state (Fig.'s. 7c-f). This trend may indicate the occurrence of the electron transfer from V^{5+} cation to form more V^{4+} sites in the V_2O_5 crystal lattice and occurring from Fe^{3+} to form more of the Fe^{2+} active sites [37-39,60,61].
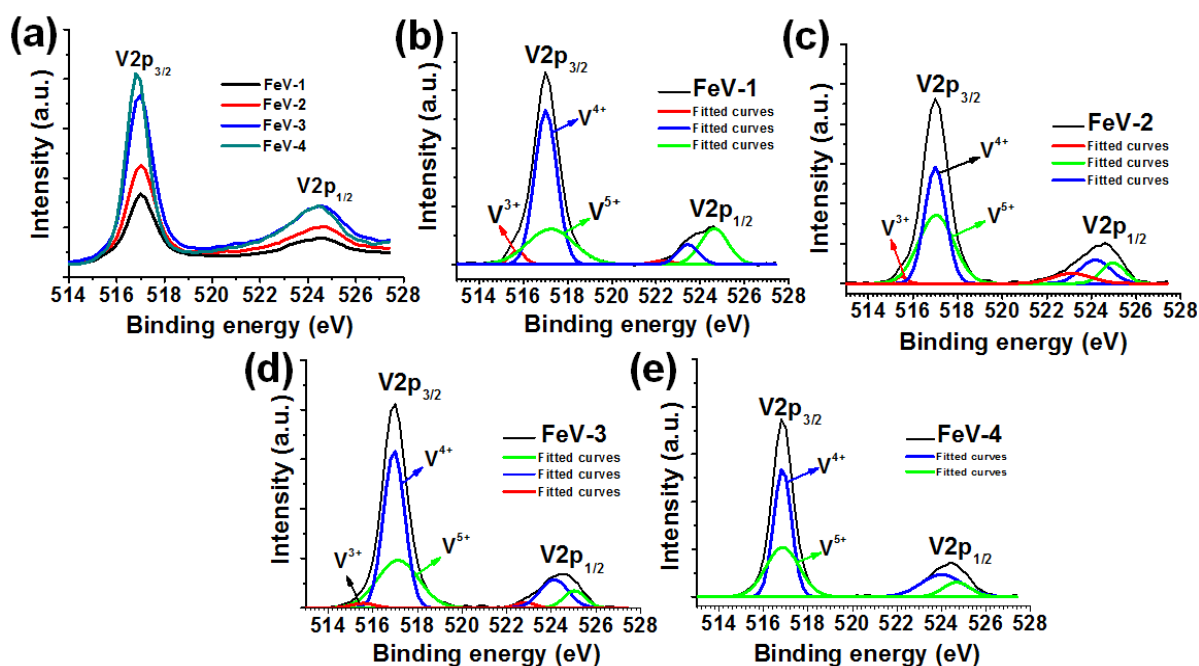
Fig. 8. V 2p XPS of (a) Overlaid FeVO$_4$ catalysts; (b) FeV-1; (c) FeV-2; (d) FeV-3; and (e) FeV-4 catalysts.

Fig. 8 shows the 2p peaks profiles of vanadium metal in the different FeVO$_4$ catalysts. The overlaid V 2p peaks of FeVO$_4$ catalysts shows peaks shifting to low BE region for FeV-4 catalyst containing the highest vanadium metal loadings while the alignment of FeV-1, FeV-2 and FeV-3 were relatively the same (Fig. 8a). Further, Fig. 6a shows the relative increase in the FeVO$_4$ catalysts peaks intensity for both the V 2p$_{2/3}$ and V 2p$_{1/2}$ at 517 eV and 524.5 eV from FeV-1 with the lowest V-metal loadings to FeV-4. The increase in the intensity of V 2p$_{3/2}$ and V 2p$_{1/2}$ peaks shows to induce the changes in the surface ratios of V^{4+}/V^{5+} oxidation states, which are associated with the different vanadium phases. The fitted V 2p peaks of the respective FeV-1 to FeV-4 catalysts are summarized in Fig.'s 9b-6e. These resolved V 2p$_{3/2}$ and V 2p$_{1/2}$ peaks shows the FeVO$_4$ catalysts with various vanadium oxidation states of V^{3+}, V^{4+} and V^{5+}. The asymmetric V 2p$_{3/2}$ signals are fitted into three peaks at BE = 515.6, 517 and 517.2 eV for all the FeVO$_4$ catalysts samples, which are attributed to the surface presence of the V^{3+}, V^{4+} and V^{5+} oxidation states [18,37,61]. The peak at 517 eV (2p$_{3/2}$) is attributed to the V^{4+} oxidation state [18]. Further, the peak intensity at $\leq$ 515.6 eV, which is ascribed to the V^{3+} oxidation state appears to decrease relatively with the increase in the vanadium loadings from FeV-1 to FeV-3. For FeV-4 catalyst with high V-metal loading, the V^{3+} shows to disappear completely with the presence of only V^{4+} and V^{5+} oxidation states detected by XPS analysis. Fig. S9 shows the high-resolution O1s peaks of the FeVO$_4$ catalysts. These O 1s peaks include the lattice oxygen (O$_L$) at BE of 529.2–529.5 eV, surface adsorbed

oxygen (O_V) at BE of 531–531.3 eV, and the adsorbed hydroxyl oxygen (O_{ads}) located at BE of 532.3–532.7 eV. The overlaid O 1s in Fig. S9(a) shows significant peaks shift of Fe_2O_3 when compared to those of $FeVO_4$. Furthermore, compared to $FeVO_4$ catalysts, the Fe_2O_3 shows high amount of O_{ads}. The $FeVO_4$ catalysts shows high amount of the oxygen vacancies (V_o) concentration compared to Fe_2O_3 catalyst. Such high oxygen vacancies could provide the enhancement in the photocatalytic performance by facilitating efficient e^-/h^+ charge generation, separation and transfer including the redox reactive sites for the improved photoactivity due to the defect structures [21,22,31,62,63].

3.2. Evaluation of photocatalytic degradation activity

3.2.1 Optimization and catalysts screening

To evaluate the MB photodegradation activity performance of $FeVO_4$ catalysts with respect to the effect of Fe:V composition, firstly the various degradation reaction conditions were optimized including the effect of (i) MB concentration; (ii) adsorption-equilibration time; (iii) catalyst activity under the photo-light and without the light; and (iv) catalyst dosage. These sets of experiments were carried out with FeV-3 catalyst based on the prior optical characterization properties. Fig. 9 shows the degradation activity of FeV-3 under the different MB concentrations in a range of 10–40 mg/L. The 10 mg/L MB shows the highest degradation efficiency of 98.7% removal of MB after 120 min of irradiation time. For 20 mg/L MB, the irradiation time of 180–210 min is required to attain 98.94% MB degradation amount while both 30 mg/L and 40 mg/L shows up to 420 min or 7h of irradiation times to attain above 95% MB degradation amounts. Dai et al. [64] explained such significant effect of MB solution concentration on its photodegradation rates, and the amount removed to be directly correlated to the photonic efficiency of the catalysts. It has been suggested that the increment of photonic efficiency with high degradation performance for low organic dye concentrations is attributed to the increase in collision frequency between the organic dye molecules and photons when compared to the decrease in high organic dye concentration, which results into poor photonic efficiency [64]. At high MB concentrations, large amount of MB dye is adsorbed on $FeVO_4$ catalyst surface, thus covering up the surface-active sites to prevent its contact with the photo-light. This could prevent the effective contact of MB dye with the radical's oxygen generated by e^-/h^+. The re-plotted Fig. 9 in Fig. S10 for equal irradiation time of 120 min shows that the effective photodegradation rates to afford shorter removal times are obtained with 10–20 mg/L MB concentrations.
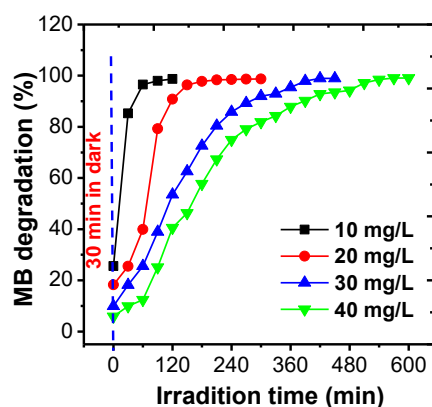
Fig. 9. Effect of MB solution concentrations on photodegradation activity of FeV-3 catalyst. Other conditions: 500 ml MB solution, pH (~7), reaction temperature (25 °C); and catalyst (100 mg).

By using 10 mg/L MB concentration, the effect of adsorption-equilibration time on the photodegradation rates (with 30 min in dark equilibration and without) was investigated. After 30 min in dark equilibration, FeV-3 degraded 23% of MB, and the amount increased to 98% after 120 min of light irradiation (Fig. 8a). For the degradation reaction carried out without prior equilibration of 30 min in dark, 98% of MB is removed within 60 min of irradiation time (Fig. 10a). The results shows that the photodegradation rates carried out without prior equilibration is more effective for FeV-3 catalyst. The differences in the degradation rates are ascribed to the fact that in the degradation with prior 30 min in dark equilibration, the surface of the catalyst active sites might be saturated with the adsorbed MB dye. The adsorbed MB could cover up the active sites, thus making the irradiation light contact with the catalyst active sites less accessible to create the effective e^-/h^+ pairs for the high photodegradation activity rates. This is corroborated by the fact that as the reaction progress for the 30 min equilibration in dark with the irradiation light switched on, there is a gradual increase in the degradation activity rates until it matches the degradation reaction rates carried out directly without prior 30 min equilibration in dark. The MB degradation activity of FeV-3 was further evaluated under both photo-irradiation light and without irradiation light. In Fig. 10b, the degradation activity of FeV-3 carried out without irradiation afforded only 30.24% of MB removal after 120 min while under irradiation light, 98.04% of MB was removed. The results show the effect of the irradiation light to contact with the catalyst active sites for creation of effective required e^-/h^+ pairs to initiate the formation degradation reactive oxygen radicals.
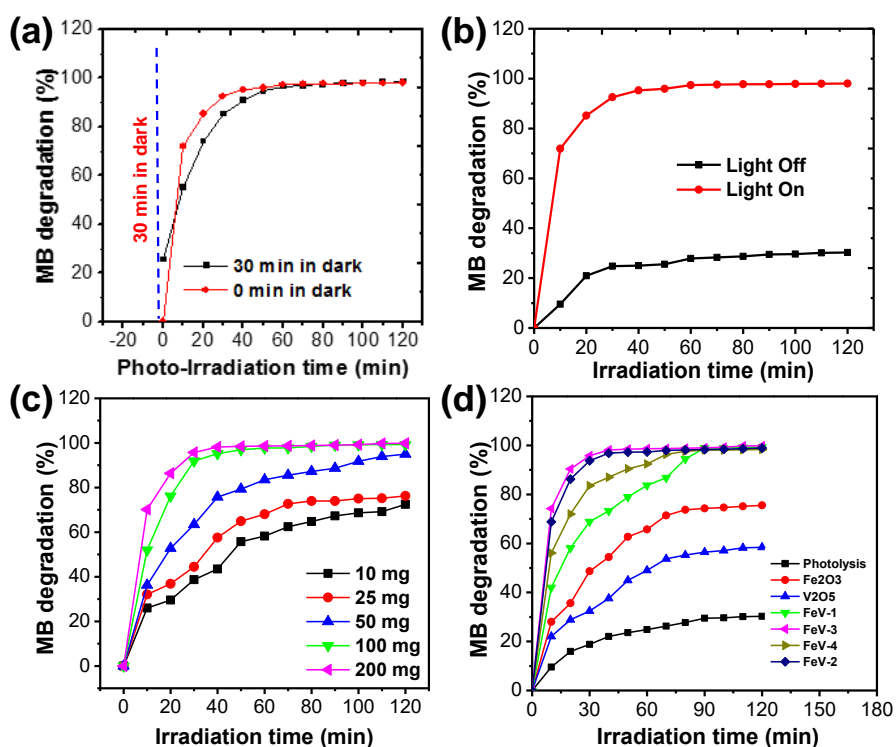
Fig. 10. (a) Composirion of 30 min equilibration in dark and without equlibration degradation rates; (b) comparison of photolysis and photo-catalysed degradation rates. (c) effect of catalyst dosage; and (d) comparison of the different FeVO$_4$ catalysts photodegradation activity. Other conditions: 500 mL MB solution; pH (~7); and reaction temperature (25 °C). (a), (b) and (d) 100 mg of catalyst amount was used. (b)–(d) 10 mg/L of MB concentration was used.

Fig. 10c shows the effect of FeV-3 catalyst dosage on MB degradation rates evaluated over a range of 10–200 mg. The removal amount of MB increased relatively from 66.19% to 98.99% with increasing catalyst dosages. The gradual increase in MB removal efficiency with increasing catalyst dosage is correlated to the high adsorption rates induced by the availability of more catalyst active sites, which could generate high amount of the effective e$^-$/h$^+$ for formation of optimized reactive oxygen radicals [65,66]. The best efficiency with respect to the amount of MB removed of about 98.3–99.0% within 40 min was achieved with 200 mg and 100 mg catalyst dosages while the least of 62% was obtained with 10 mg dose at irradiation time of 120 min (Fig. 10c). While the increase in FeV-3 dosage (i.e., 100 and 200 mg) showed to increase the degradation rates and amount removed of MB, it also indicated that once the maximum FeV-3 dosage was reached, further increase in the dosage was not providing any significant increase in rates and removal amount of MB. This observation can be explained by the fact that when more than adequate catalyst dose is added, the solution becomes more turbid, which causes

18

the photo-light to become difficult to go through the water. As a result, large quantities of catalyst could not be irradiated by light in more than adequate dosage exceeding equilibrium, thus photonic efficiency decreases with a large insignificant catalyst dosage quantity [67].

Fig. 10d shows the results for the effect of various Fe:V compositions on photodegradation activity of $FeVO_4$ catalysts for MB removal efficiency. The single V_2O_5 and Fe_2O_3 oxide shows low photodegradation activity when compared to the binary $FeVO_4$ catalysts with both affording MB removal amounts of 57.44% and 75.29%, respectively after 120 min. For $FeVO_4$ catalysts, their photodegradation activity for MB removal increased relatively with the increase in V-metal loadings from FeV-1 to FeV-4. After 120 min, all the $FeVO_4$ catalysts achieved near complete MB removal (Fig. 10d). However, the comparison of the $FeVO_4$ catalysts at irradiation time of 50 min (Fig. S11), they show the MB degradation amounts of 78.93% (FeV-1), 90.41% (FeV-2), 98.46% (FeV-3), and 97.84% (FeV-4). This demonstrate that both FeV-3 and FeV-4 catalysts requires less photo-irradiation times of up to 30 min to achieve high degradation rates efficiency. The results shows that there is a direct influence of vanadium metal composition amount on the photodegradation activity rates of the $FeVO_4$ based catalyst. In particular, the results shows that the photocatalytic activity rates improve relatively with the increasing amounts of V-metal loadings according to the determined elemental compositions amounts (Table S1-S6 and Fig. S3-S6). In fact, the increasing activity of the $FeVO_4$ based catalysts with the relative increase in V-metal loadings correlated well with the structure evolution formation of the $FeVO_4$ phase from pure Fe_2O_3 and low loadings of V-metal to the high loaded V-metal amounts (Fig. 1). Based on the XRD results, the formation of $FeVO_4$ structure phase was clear for the FeV-3 (~ 27 wt%) and FeV-4 (~ 34 wt%). Both FeV-3 and FeV-4 were the catalysts with the highest degradation rates for the removal of MB, thus the reduced photo-irradiations times of up to 30 min when compared to the others that required more than 100 min. According to the PL results, the FeV-3 shows the lowest intensity when compared to the other binary $FeVO_4$ catalysts, including both the Fe_2O_3 and V_2O_5. The PL results correlated well with the obtained degradation activity performances trends of the different $FeVO_4$ catalysts where FeV-3 with the best e^-/h^+ generation and separation efficiency, thus suppressed recombination rates shows the highest photocatalytic degradation activity rates than the others did. Another aspect worth mentioning is the probable influence of the vanadium oxidation state. According to the XPS high resolution of V 2p (Fig. 7 and Fig. S9), vanadium was obtained with its three common oxidation states of V^{3+}; V^{4+} and V^{5+} for the FeV-1 and FeV-2 catalysts while FeV-3 shows trace amounts and FeV-4 showed completely no detectable V^{3+}. With reference to supported vanadium metal catalysts, the most active catalyst had been found to compose of V^{4+} and V^{5+} oxidation states [58]. Perhaps, the

presence of the low V^{3+} oxidation state could also contribute to the low photo-activity of $FeVO_4$ (i.e., FeV-1 and FeV-2) in conjunction to the absence of the well-defined formed orthovanadate structure phase. In particular, the V^{4+} has been shown to present the highly active vanadium catalysts in several catalytic reactions, which is correlated to its reactive coordinated electronic structure associated with the monolayer VO_4. The VO_4 structure is the building block of the binary $FeVO_4$ structure framework, and thus its interaction with the Fe can induce modified electronic structure, which would influence the band gap energies and optics of the different binary $FeVO_4$ catalysts. Such profound electronic structure modification of the $FeVO_4$ catalysts were observed by XPS shifting of both Fe and V respectively with increasing amounts of V-metal loadings. These comprehensive structure properties show to be significant in understanding the design and photocatalytic performance application of the $FeVO_4$ based catalysts. During photocatalysis reaction process, V^{4+} can act as e^- and h^+ trapping sites which can favour charge effective separation, while V^{5+} might act as an electron acceptor for the enhanced photodegradation activity [69]. This prominent effect of V^{4+}/V^{5+} structure composition modulation in $FeVO_4$ could be significant for manifesting the design of its improved photocatalytic activity performances. Moreover, another contributing factor on the observed high photodegradation activity of FeV-3 catalyst compared to others is the effect of the formed heterojunction interface of $Fe_2O_3/FeVO_4$ phases in FeV-3. The formation of such heterostructure interface was confirmed by the XRD and Raman results. The presence of both Fe_2O_3 and $FeVO_4$ in $FeVO_4$ derived materials has been demonstrated previously to be efficient photocarriers charge separation and transfer, thus minimizing the recombination rates as confirmed in the PL (Fig. 5c) and EIS (Fig. 6b) results [70–72].

The influence of scavengers on control experiments to study the type of active species accounting for the catalytic photodegradation activity of MB were evaluated using FeV-3 catalyst. Fig. 11a illustrate the trapping using the different scavengers for probing electrons (e^-), holes (h^+) superoxide anion radicals ($O_2^{\bullet-}$), and hydroxyl radicals ($OH^{\bullet-}$) reactive species. The catalytic photodegradation amount of MB was only 43% from 98.2% when triethanolamine (TEOA) was added as h^+ scavengers, which showed that h^+ is playing a significant role in accelerating the photocatalytic activity. Moreover, the addition of isopropanol (IPA) as $^{\bullet}OH$ scavengers demonstrated a significant decrease in the amount of degraded MB from 98.2% to 39%, while Benzoquinone (BQ) addition for $^{\bullet}O_2$ showed minimal decrease from 98.2% to 88.6% of MB removal efficiency. This showed that the formation and presence of h^+ and $^{\bullet}OH$ species were primarily important to create effective photocatalytic reactive system conditions for the efficient degradation of MB than negligible effect of $^{\bullet}O_2$ radicals. Based on the photocatalytic tests and characterisation results, tentative proposed mechanism of heterostructure $Fe_2O_3/FeVO_4$ (FeV-3) catalyst operation in the photodegradation of MB is illustrated by Fig. 11 [70-73]. Moreover, the

reusability and stability of $Fe_2O_3/FeVO_4$ (FeV-3) catalyst thus decrease of its activity was evaluated for five times repeatable test experiments of MB degradation reactions. Insignificant decrease of MB degradation efficiency was observed with removal amount stabilized within 97–99%.
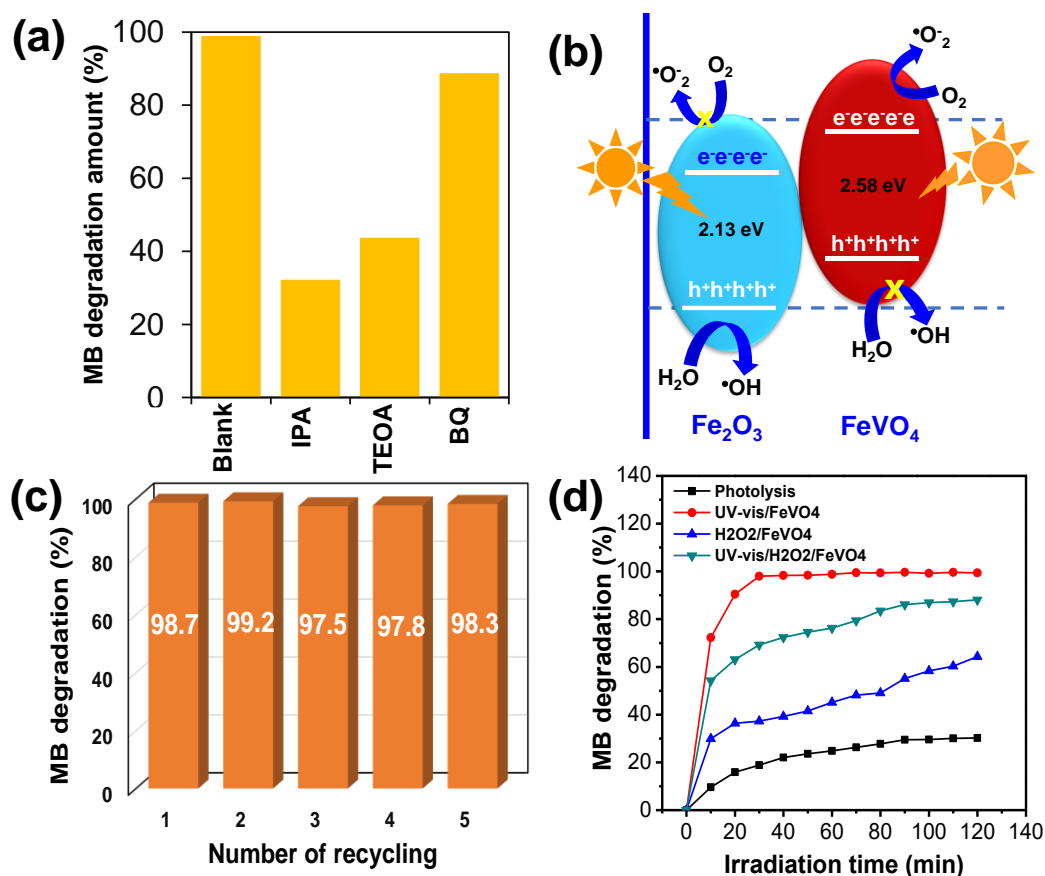

Fig.11. (a) Trapping experiments of reactive species in MB photodegradation reaction. (b) Representation of redox potential of $FeVO_4$ and Fe_2O_3 heterostructure to generate reactive oxygen species of $^{\bullet}OH$ and $^{\bullet}O_2^-$ radicals. (c) Recyclability performance of FeV-3 catalyst. (d) Evaluation of FeV-3 catalyst degradation activity under photo, Fenton and photo-Fenton conditions Other conditions: 500 mL MB solution; solutionn concentration (10 mg/L); solution pH (~7); catalyst amount (100 mg); and irradiation time (120 min).

3.2.2 Comparison of Fenton, photo and photo-Fenton activity of $FeVO_4$

Fig. 11d shows the MB photodegradation activity of FeV-3 under the three different AOPs (i.e., Fenton, photo, and photo-Fenton). All these processes use the ROS derived hydroxyl free radicals driven mechanism as an effective degradation path but differ from the routes to produce them. The results show

the combination of photo-light and FeV-3 catalyst to give the best degradation rates performance by achieving up to 98% of MB removal after comparable photo-irradiation time of 120 min. This was followed by the photo/H_2O_2/FeV-3 system as the second best to afford up to 88% of MB removal after 120 min while Fenton-like system (i.e., H_2O_2/FeV-3) could only reach up to 64% of MB removal. The less MB degradation activity of H_2O_2/FeV-3 Fenton system might arise from molar ratio of Fenton reagent (H_2O_2 and Fe (II)) since it has been reported to be an essential operating factor to determine the dye removal efficiency because either of the two chemicals can scavenge the in-situ reaction formed $^\cdot$OH radical [74]. Further, Fenton processes is mostly effective in the acidic pH solution medium, typically 3–4 pH [74]. The use of H_2O_2 also affect the activity of UV/H_2O_2/FeV-3 process since it requires a continuous dose of H_2O_2 oxidant, which disadvantages the utilization of UV/H_2O_2 AOP, since only around 20% of H_2O_2 is consumed during the AOPs [75]. Hence, this led to the requirement of quenching step of the residuals excess H_2O_2 using sodium thiosulphate sodium hypochlorite or granular activated carbon [76]. The use of these metal salts to quench the residual H_2O_2 can result into formation of environmentally unfriendly inorganic wastes that will require further work up for safe disposal, increasing on additional costs in the process operation.

5. Conclusions

In summary, we demonstrated the synthesis of binary $FeVO_4$ catalysts with various vanadium (V) loading amounts of 10% (FeV-1); 20 wt% (FeV-2); 30 wt% (FeV-3) and 40 wt% (FeV-4) using the sol-gel surfactant assisted method. The structure evolution developments of $FeVO_4$ relating to the crystallinity and phases compositions, morphology, textural, electronic, interactions, oxidation state and optical properties were studied by using XRD, PL, SEM, FTIR, XPS and BET surface areas techniques. The formation of morphology consisting of nanoparticles was confirmed with the particle size increasing relatively with the increase in vanadium loading. Similarly, the crystallinity and phase formation of $FeVO_4$ showed to depend on the amount of vanadium loading. Further, the catalysts were also showed the modifications of the electronic and optical absorbance structure properties with respect to V-metal loadings that was accompanied by noticeable peaks shifting in both XRD and XPS. The FeV-3 showed the best photocatalytic performance and its performance and other heterostructure $FeVO_4$ catalysts correlated well with the obtained catalytic results. The results showed that there is a direct influence of the vanadium metal loading of the photocatalytic performance of the $FeVO_4$ catalyst. Further, the results showed that an optimum loading of V in $FeVO_4$ is critical to achieve the high photodegradation rates. In particular, the catalyst with both Fe_2O_3 and $FeVO_4$ phases forming heterojunction showed to provide effective surface activity for the efficient photocarriers separation and charge transfer with less recombination, thus enhance photocatalytic performance.

Acknowledgements

CRediT authorship contribution statement

Kgabo P. Thaba: Formal analysis, Methodology, Investigation, Writing-original draft, Visualization.

Mabel M. Mphahlele-Makgwane: Conceptualization, Investigation, Validation, Resources, Funding acquisition, Writing-review & editing, Supervision, Project administration.

Pannan I. Kyesmen: Investigation, Formal analysis, Writing-review & editing.

Mmantsae Diale: Formal analysis, Writing-review & editing

Priscilla G. Baker: Formal analysis, Writing-review & editing

Peter R. Makgwane: Conceptualization, Validation, Writing-original draft, Writing-review & editing, Supervision.

Declaration of Competing Interest

The authors declare that they have no known competing financial interests or personal relationships that could have appeared to influence the work reported in this paper.

Conflicts of Interest

The authors declare no conflict of interest. The funders had no role in the design of the study; in the collection, analyses, or interpretation of data; in the writing of the manuscript, or in the decision to publish the results.

References

[1] H. Schweppe, Identification of dyes in historic textile materials (In) Historic textile and paper materials, Chapter 8, Advances in Chemistry, 21 (1986) 153-174.

[2] S. Moosavi, C.W. Lai, S. Gan, G. Zamiri, O.A. Pivehzhani, M.R. Johan, Application of efficient magnetic particles and activated carbon for dye removal from wastewater, ACS Omega 5(33) (2020) 20684–20697.

[3] U. Ghimire, G. Sarpong, V.G. Gude, Transitioning wastewater treatment plants toward circular economy and energy sustainability, ACS Omega 6(18) (2021) 11794–11803.

[4] P. Samanta, A.V. Desai, S. Let, S.K. Ghosh, Advanced porous materials for sensing, capture and detoxification of organic pollutants toward water remediation, ACS Sustain. Chem. Eng. 7(8) (2019) 7456–7478.

[5] H. Dai, X. Yuan, L. Jiang, H. Wang, J. Zhang, J. Zhang, T. Xiong, Recent advances on ZIF-8 composites for adsorption and photocatalytic wastewater pollutant removal: Fabrication, applications and perspective, Coord. Chem. Rev. 442 (2021) 213985.

[6] C.Y. The, P.M. Budiman, K.Y. Shak, T.Y. Wu, Recent advancement of coagulation-flocculation and its application in wastewater Treatment, Ind. Eng. Chem. Res. 55(16) (2016) 4363–4389.

[7] S. Mustafa, H.N. Bhatti, M. Maqbool, M. Iqbal, Microalgae biosorption, bioaccumulation and biodegradation efficiency for the remediation of wastewater and carbon dioxide mitigation: Prospects, challenges and opportunities, J. Water Process Eng. 41 (2021) 102009.

[8] D. Ma, H. Yi, C. Lai, X. Liu, X. Huo, Ziwen An, L. Li, Y. Fu, B. Li, M. Zhang, L. Qin, S. L. Yang, Critical review of advanced oxidation processes in organic wastewater treatment, Chemosphere 275 (2021) 130104.

[9] L. Liu, Z. Chen, J. Zhang, D. Shan, Y. Wu, L. Bai, B. Wang, Treatment of industrial dye wastewater and pharmaceutical residue wastewater by advanced oxidation processes and its combination with nanocatalysts: A review, J. Water Process Eng. 42 (2021) 102122.

[10] K. Kannan, D. Radhika, K.K. Sadasivuni, K.R. Reddy, A.V. Raghu, Nanostructured metal oxides and its hybrids for photocatalytic and biomedical applications, Adv. Colloid Interf. Sci. 281 (2020) 102178

[11] T.S. Natarajan, K.R. Thampi, R.J. Tayade, Visible light driven redox-mediator-free dual semiconductor photocatalytic systems for pollutant degradation and the ambiguity in applying Z-scheme concept, Appl. Catal. B: Environ. 227 (2018) 296–311

[12] Swagata Banerjee, S.C. Pillai, P. Falaras, K.E. O'Shea, J.A. Byrne, D.D. Dionysiou, New insights into the mechanism of visible light photocatalysis, J. Phys. Chem. Lett. 5(15) (2014) 2543–2554.

[13] E. Ovodok, H. Maltanava, S. Poznyak, M. Ivanovskaya, V. Shendyukov, V. Spacek, N. Scharnagl, F. Maia, J. Tedim, Rhodamine-loaded TiO_2 particles for detection of polymer coating UV degradation, Mater. Today: Proc. 20 (2020) 320–328.

[14] B.G. Aliabadi, N. Gilani, J.V. Pasikhani, A.E. Pirbazari, Boosting the photoconversion efficiency of TiO_2 nanotubes using UV radiation-assisted anodization as a prospective method: An efficient photocatalyst for eliminating resistant organic pollutants, Ceram. Int. 46 (2020) 19942–19951.

[15] S.S. Nkosi, I.Kortidis, D.E. Motaung, P.R. Makgwane, O.M. Ndwandwe, S.S. Ray, G. Kiriakidis, An instant photo-excited electrons relaxation on the photo-degradation properties of TiO_{2-x} films, J. Photochem. Photobio. A: Chem. 293 (2014) 72–80.

[16] P.A.Luque, H.E. Garrafa-Gálvez, O. Nava, A.Olivas, M.E. Martínez-Rosas, A.R. Vilchis-Nestor, A. Villegas-Fuentes, M.J. Chinchillas-Chinchillas, Efficient sunlight and UV photocatalytic degradation of methyl orange, methylene blue and Rhodamine B, using Citrus×paradisi synthesized SnO_2 semiconductor nanoparticles, Ceram. Int. Available online 14 May 2021, In Press, Corrected Proof

[17] S. Yadav, N. Kumar, V. Kumari, A. Mittal, S. Sharma, Photocatalytic degradation of triclopyr, a persistent pesticide by ZnO/SnO_2 nano-composites, Mater. Today: Proc. 19 (2019) 642–645.

[18] M.M. Sajid, N.A. Shad, Y. Javed, S.B. Khan, Z. Zhang, N. Amin, H. Zhai, Preparation and characterization of vanadium pentoxide (V_2O_5) for photocatalytic degradation of monoazo and diazo dyes, Surf. Interf. 19 (2020) 100502.

[19] C.N.C. Hitam, A.A. Jalil, A review on exploration of Fe_2O_3 photocatalyst towards degradation of dyes and organic contaminants, J. Environ. Manage. 258 (2020) 110050.

[21] Z. Wang, Z. Lin, S. Shen, W. Zhong, S. Cao, Advances in designing heterojunction photocatalytic materials, Chin. J. Catal. 42 (2021) 710–730.

[22] J. Low, C. Jiang, B. Cheng, S. Wageh, A.A. Al-Ghamdi, J. Yu, A review of direct Z-scheme photocatalysts, Small Methods, 1 (2017) 1700080.

[23] R.M. Hegazey, E.A. Abdelrahman, Y.H. Kotp, A.M. Hameed A. Subaihi, Facile fabrication of hematite nanoparticles from Egyptian insecticide cans for efficient photocatalytic degradation of rhodamine B dye, J. Mater. Res. Technol. 9 (2020) 1652–1661.

[24] Y. Tong, S. Zhao, J. Kang, J. Shen, Z. Chen, B. Wang, L. Bi, J. Deng, Preparation of small-sized $BiVO_4$ particles with improved photocatalytic performance and its photocatalytic degradation of doxycycline in water, Colloids Surf. A: Physicochem. Eng. Aspects, 620 (2021) 126412.

[25] T. Munawar, S. Yasmeen, F. Hussain, K. Mahmood, A. Hussain, M. Asghar, Synthesis of novel heterostructured ZnO-CdO-CuO nanocomposite: Characterization and enhanced sunlight driven photocatalytic activity, Mater. Chem. Phys. 249 (2020) 122983.

[26] F.A. Hezam, O. Nur, M.A. Mustafa, Synthesis, structural, optical and magnetic properties o $NiFe_2O_4$/MWCNTs/ZnO hybrid nanocomposite for solar radiation driven photocatalytic degradation and magnetic separation, Colloids Surf. A: Physicochem. Eng. Aspects, 592 (2020) 124586.

[27] S. Kappadan, S. Thomas, N. Kalarikkal, $BaTiO_3$/ZnO heterostructured photocatalyst with improved efficiency in dye degradation, Mater. Chem. Phys. 255 (2020) 123583.

[28] T. Munawar, F. Iqbal, S. Yasmeen, K. Mahmood, A. Hussain, Multi metal oxide NiO-CdO-ZnO nanocomposite–synthesis, structural, optical, electrical properties and enhanced sunlight driven photocatalytic activity, Ceram. Int. 46 (2020) 2421–2437.

[29] Z. Wu, Y. Xue, X. He, Y. Li, X. Yang, Z. Wu, G. Cravotto, Surfactants-assisted preparation of $BiVO_4$ with novel morphologies via microwave method and CdS decoration for enhanced photocatalytic properties, J. Hazard. Mater. 387 (2020) 122019

[30] S. Sharma, A. Mittal, N.S. Chauhan, P.R. Makgwane, K. Kumari, S. Maken, N. Kumar, Developments in visible-light active TiO_2/SnX (X = S and Se) and their environmental photocatalytic applications – A mini-review, Inorganic Chemistry Communications, 133 (2021) 108874

[31] S. Sharma, N. Kumar, P.R. Makgwane, N. S. Chauhan, K. Kumari, M. Rani, S. Maken, TiO_2/SnO_2 nano-composite: New insights in synthetic, structural, optical and photocatalytic aspects, Inorganica Chimica Acta, (2021) 120640. In Press, https://doi.org/10.1016/j.ica.2021.120640

[32] M. Wang, X. Hu, Z. Zhan, T. Sun, Y. Tang, Facile fabrication of $CeVO_4$ hierarchicalhollow microspheres with enhanced photocatalytic activity, Mater. Lett. 253 (2019) 259–262.

[33] I. Shafiq, M. Hussain, R. Rashid, S. Shafique, P. Akhter, W. Yang, A. Ahmed, Z. Nawaz, Y.-K. Park, Development of hierarchically porous $LaVO_4$ for efficient visible light-driven photocatalytic desulfurization of diesel, Chem. Eng. J. 420 (2021) 130529.

[34] N. Wetchakun, P. Wanwaen, S. Phanichphant, K. Wetchakun, Influence of Cu doping on the visible-light-induced photocatalytic activity of $InVO_4$, RSC Adv. 7 (2017) 13911–13918.

[35] P. Shandilya, D. Mittal, A. Sudhaik, P. Raizada, A.K. Saini, P. Singh, $GdVO_4$ modified fluorine doped graphene nanosheets as dispersed photocatalyst for mitigation of phenolic compounds in aqueous environment and bacterial disinfection, Sep. Purif. Technol. 210 (2019) 804–816.

[36] R. Monsef, M. Ghiyasiyan-Arani, O. Amiri, M. Salavati-Niasari, Sonochemical synthesis, characterization and application of $PrVO_4$ nanostructures as an effective photocatalyst for discoloration of organic dye contaminants in wastewater, Ultrason. Sonochem. 61 (2020) 104822.

[37] M.M. Sajid, H. Zhai, N.A. Shad, M. Shafique, A.M. Afzal, Y. Javed, S.B. Khan, M. Ikram, N. Amin, Z. Zhang, Photocatalytic performance of ferric vanadate ($FeVO_4$) nanoparticles synthesized by hydrothermal method, Mater. Sci. Semicon. Process. 129(2021) 105785.

[38] Q. Liu, J. Zhao, Y. Wang, Y. Liu, J. Dong, J. Xia, H. Li, The novel photo-Fenton-like few-layer MoS_2/$FeVO_4$ composite for improved degradation activity under visible light irradiation, Colloids Surf. A: Physicochem. Eng. Aspects, 623 (2021) 126721.

[39] S.R. Setayesh, P. Nazari, R. Maghbool, Engineered $FeVO_4$/CeO_2 nanocomposite as a two-way superior electro-Fenton catalyst for model and real wastewater treatment, J. Environ. Sci. 97 (2020) 110–119.

[40] M.M. Sajid, N.A. Shad, Y. Javed, S.B. Khan, Z. Zhang, N. Amin, H. Zhai, Morphological effects on the photocatalytic performance of FeVO$_4$ nanocomposite, Nano-Struct. Nano-Objects, 22 (2020) 100431.

[41] B. Ozturk, G.S.P. SOYLU, Synthesis of surfactant-assisted FeVO$_4$ nanostructure: Characterization and photocatalytic degradation of phenol, J. Mol. Catal. A: Chem. 398 (2015) 65–71.

[42] R. Rahimpour, N. Chaibakhsh, M.A. Zanjanchi, Z. Moradi-Shoeili, Fabrication of ZnO/FeVO$_4$ heterojunction nanocomposite with high catalytic activity in photo-Fenton-like process, J. Alloys Compds, 817 (2020) 152702

[43] A.Š. Vuk, B. Orel, G. Dražič, F. Decker, P. Colomban, UV-Visible and IR Spectro electrochemical studies of FeVO$_4$ sol-gel films for electrochromic applications. J. Sol Gel Sci. Technol. (2002) 165–181.

[44] A. Kumar, G. Sharma, M.F. Naushad, J. Stadler, A.A. Ghfar, P. Dhiman, R.V. Saini, Sustainable nano-hybrids of magnetic biochar supported g-C$_3$N$_4$/FeVO$_4$ for solar powered degradation of noxious pollutants-Synergism of adsorption, photocatalysis & photo-ozonation. J. Clean. Prod. 165 (2017) 431–451.

[45] Q. Nong, M. Cui, H. Lin, L. Zhao, Y. He, Fabrication, characterization and photocatalytic activity of g-C$_3$N$_4$ coupled with FeVO$_4$ nanorods, RSC Adv. 5 (2015) 27933–27939.

[46] M.M. Sajid, S.B. Khan, N.A. Shad, N. Amin, Z. Zhang, Visible-light assisted photocatalytic degradation of crystal violet dye and electrochemical detection of ascorbic acid using a BiVO$_4$/FeVO$_4$ heterojunction composite, RSC Adv. 8 (2018) 23489–23498.

[47] Y. Tang, J. Kang, M. Wang, C. Jin, J. Liu, M. Li, S. Li, Z. Li, Catalytic degradation of oxytetracycline via FeVO$_4$ nanorods activating PMS and the insights into the performance and mechanism, J. Environ. Chem. Eng. 9 (2021) 105864.

[48] M. Khalfaoui, S. Knani, M.A. Hachicha, A.B. Lamine, New theoretical expressions for the five adsorption type isotherms classified by BET based on statistical physics treatment. J. Colloid Interf. Sci. 263(2) (2003) 350–356.

[49] P.M. Malibo, P.R. Makgwane, P.G. Baker, Heterostructured redox-active V$_2$O$_5$/SnO$_2$ oxide nanocatalyst for aqueous-phase oxidation of furfural to renewable maleic acid, ChemistrySelect, 5 (2020) 6255-6267.

[50] J.A. Martín-Martín, M. Gallastegi-Villa, M.P. Gonźalez-Marcos, A. Aranzabal, J. R. Gonźalez-Velasco, Bimodal effect of water on V$_2$O$_5$/TiO$_2$ catalysts with different vanadium species in the simultaneous NO reduction and 1,2-dichlorobenzene oxidation Chem. Eng. J. 417 (2021) 129013

[51] V.V. Kaichev, Y.A. Chesalov, A.A. Saraev, A.Y. Klyushin, A. Knop-Gericke, T.V. Andrushkevich, V.I. Bukhtiyarov, Redox mechanism for selective oxidation of ethanol over monolayer V$_2$O$_5$/TiO$_2$ catalysts, J. Catal. 338 (2016) 82-93

[52] Makgwane, P.R., Ferg, E.E., Billing, D.G. et al. Liquid Phase Oxidation of p-cymene by $(VO)_2P_2O_7$ and $VO(PO_3)_2$ Catalysts. Catal. Lett. 135, 105–113 (2010).

[53] H. Mandal, S. Shyamal, P. Hajra, A. Bera, D. Sariket, S. Kundu, C. Bhattacharya, Development of ternary iron vanadium oxide semiconductors for applications in photoelectrochemical water oxidation, RSC Adv. 6 (2016) 4992-4999.

[54] C.D. Morton, I.J. Slipper, M.J. K. Thomas, B.D. Alexander, Synthesis and characterisation of Fe–V–O thin film photoanodes, J. Photochem. Photobiol. A: Chem. 216 (2010) 209-214.

[55] M.M. Sajid, H. Zhai, N. Akhtar Shad, M. Shafique, A.M. Afzal, Y. Javed, S.B. Khan, M. Ikram, N. Amin, Z. Zhang, Photocatalytic performance of ferric vanadate ($FeVO_4$) nanoparticles synthesized by hydrothermal method, Materials Science in Semiconductor Processing, 129 (2021) 105785.

[56] A.Š. Vuk, B. Orel, G. Dražič, F. Decker, P. Colomban, UV-Visible and IR Spectroelectrochemical studies of $FeVO_4$ Sol-Gel films for electrochromic applications, J. Sol-gel Sci. Technol. 23(2) (2002) 165–181.

[57] G. Kesavan, M. Pichumani, S.-M. Chen, Influence of crystalline, structural, and electrochemical properties of iron vanadate nanostructures on flutamide detection, ACS Appl. Nano Mater. 4(6) (2021) 5883–5894

[58] B. Saravanakumar, N. Karthikeyan, P.A. Periasamy, A.J. Britten, M. Mkandawire, Polyethylene glycol mediated synthesis of iron vanadate ($FeVO_4$) nanoparticles with supercapacitive features, Mater. Res. Express 7 (2020) 064010.

[59] M.M. Sajid, S.B. Khan, N.A. Shad, N. Amin, Z. Zhang, Visible light assisted photocatalytic degradation of crystal violet dye and electrochemical detection of ascorbic acid using a $BiVO_4$/$FeVO_4$ heterojunction composite, RSC Adv. 8 (2018) 23489

[60] M.A. Mavuso, P.R. Makgwane, S.S. Ray, Heterostructured CeO_2-M (M = Co, Cu, Mn, Fe, Ni) oxide nanocatalysts for the visible-light photooxidation of pinene to aroma oxygenates, ACS Omega 5(17) (2020) 9775-9788

[61] D. Flak, Q. Chen, B.S. Mun, Z. Liu, M. Rękas, A. Braun, In situ ambient pressure XPS observation of surface chemistry and electronic structure of α-Fe_2O_3 and γ-Fe_2O_3 nanoparticles, Appl. Surf. Sci. 455 (2018) 1019-1028.

[62] Q. Wang, Z. Liu, Q. Lu, E. Guo, M. Wei, Fabrication of direct Z-scheme α-Fe_2O_3/$FeVO_4$ nanobelts with enhanced photoelectrochemical performance, ChemistrySelect, 3(2) (2018) 809–815.

[63] Y. Chen, W. Yang, S. Gao, C. Sun, Q. Li, Synthesis of Bi_2MoO_6 nanosheets with rich oxygen vacancies by post-synthesis etching treatment for enhanced photocatalytic performance, ACS Appl. Nano Mater. 1 (7) (2018) 3565–3578.

[64] L. Paramanik, K.H. Reddy, K.M. Parida, Stupendous photocatalytic activity of p-BiOI/n-PbTiO$_3$ heterojunction: The significant role of oxygen vacancies and interface coupling, J. Phys. Chem. C 123 (35) (2019) 21593–21606.

[65] K. Dai, L. Lu, G. Dawson, Development of UV-LED/TiO$_2$ device and their application for photocatalytic degradation of methylene blue, J. Mater. Eng. Perform. 22(4) (2013) 1035–1040.

[66] V.K. Gupta, R. Jain, M.N. Siddiqui, T.A. Saleh, S. Agarwal, S. Malati, Equilibrium and thermodynamic studies on the adsorption of the dye rhodamine-B onto mustard cake and activated carbon. J. Chem. Eng. Data, 55 (2010) 5225–5229.

[67] M. Salehi, H. Hashemipour, M. Mirzaee, Experimental study of influencing factors and kinetics in catalytic removal of methylene blue with TiO$_2$ nanopowder, Am. J. Environ. Eng. 2(1) (2012) 1–7

[68] R.J. Wu, C.C. Chen, M.H. Chen, C.S. Lu, Titanium dioxide-mediated heterogeneous photocatalytic degradation of terbufos: Parameter study and reaction pathways. J. Hazard. Mater. 162(2-3) (2009) 945–953.

[69] J. Yu, A. Kudo, Effects of structural variation on the photocatalytic performance of hydrothermally synthesized BiVO$_4$, Adv. Funct. Mater. 16(16) (2006) 2163–2169.

[70] Q. Wang, Z. Liu, Q. Lu, E. Guo, M. Wei, Fabrication of Direct Z-scheme α-Fe$_2$O$_3$/FeVO$_4$ Nanobelts with Enhanced Photoelectrochemical Performance, ChemistrySelect, 3 (2018) 809–815.

[71] Binary and ternary vanadium oxides: General overview, physical properties, and photochemical processes for environmental applications, O. Monfort, P. Petrisková, Processes 9(2) (2021) 214.

[72] H. Mandal, S. Shyamal, P. Hajra, A. Bera, D. Sariket, S. Kundu, C. Bhattacharya, Development of ternary iron vanadium oxide semiconductors for applications in photoelectrochemical water oxidation, RSC Adv., 2016,6, 4992-4999.

[73] C. Zhao, G. Tan, W. Yang, Fast interfacial charge transfer in α-Fe$_2$O$_{3-\delta}$C$_\delta$/FeVO$_{4-x+\delta}$C$_{x-\delta}$@C bulk heterojunctions with controllable phase content. Sci Rep 6 (2016) 38603.

[74] P.D. Swaim, R. Morgan, P. Mueller, M. Vorissis, U. Erdal, W. Carter, Implementing an effective UV advanced oxidation process, Proceedings of the Water Environment Federation, 1 (2009) 678–688.

[75] O.S. Keen, A.D. Dotson, K.G. Linden, Evaluation of hydrogen peroxide chemical quenching agents following an advanced oxidation process. J. Environ. Eng. 139(1) (2012) 137–140.

[76] J.C. Kruithof, P.C. Kamp, B.J. Martijn, UV/H$_2$O$_2$ treatment: a practical solution for organic contaminant control and primary disinfection. Ozone Sci. Eng. 29(4) (2007) 273–280.